ELSEVIER

Contents lists available at ScienceDirect

Computational Materials Science

journal homepage: www.elsevier.com/locate/commatsci



Full Length Article

Simulation of high strain rate contact of single crystal Al spheres

Tanish Kothapalle ^a, Aneesh V. Melachuri ^a, James J. Rogers ^a, Kien Bach Tran ^a, Michael F. Becker ^{b,c,d,*}, Desiderio Kovar ^{a,c,d}

- ^a Walker Department of Mechanical Engineering, The University of Texas at Austin, Austin, TX 78712, USA
- ^b Chandra Family Department of Electrical and Computer Engineering, The University of Texas at Austin, Austin, TX 78712, USA
- ^c Materials Science and Engineering Program, The University of Texas at Austin, Austin, TX 78712, USA
- ^d Center for Additive Manufacturing and Design Innovation, The University of Texas at Austin, Austin, TX 78712, USA

ARTICLE INFO

Keywords: Nanoparticle mechanics Molecular dynamics High strain rate deformation

ABSTRACT

Nanoindentation is used to probe mechanical properties of materials on a small size scale, and it is normally conducted under quasi-static conditions or at relatively low strain rates that are governed by experimental limitations. Using molecular dynamics (MD) simulations, we can now study similar contact events at strain rates up to $\sim 1 \times 10^{12}~\rm s^{-1}$. At these high strain rates, additional deformation mechanisms, such as atomic amorphization and viscous flow, are anticipated. Here, we report MD simulations of 6 nm diameter, single-crystal aluminum (Al) spheres contacted by a rigid plate moving at velocities from 10 to 1000 m/s. Both global variables (force versus displacement) and atomic variables (dislocation activity, amorphization, and potential energy per atom) are measured as the sphere experiences plastic deformation. These measurements allow global and atomistic behavior to be correlated in a well-controlled simulation. At lower contact velocities, we observe that plastic deformation is dominated by dislocation activity accompanied by load drops. At higher contact velocities, the load drops disappear, and stiffening is observed. This behavior is accompanied by decreasing dislocation lengths and increasing numbers of atoms that are in the amorphous state and that deform via viscous flow. Dislocation-dominated deformation that occurs during the initial stages of deformation even at high contact velocities is found to play an important role in determining the final state of the sphere even when the original dislocations and previously disordered atoms have annealed.

1. Introduction

Indentation is a common way to probe mechanical parameters of a macroscopic sample because it is an intuitive and straightforward experiment to perform, and the results are relatively straightforward to interpret. The test is conducted by slowly varying a global control (load) while monitoring a global variable (depth of indentation). These are global controls and variables because they are applied and monitored at the spatial scale of the indenter and thus provide access to macroscopic mechanical parameters. The control is applied uniformly to the indenter and the response of the variable depends on the overall response of the material being indented. The indenter is commonly a sphere, cylinder, cone, or pyramid; and the relatively low strain rates that are applied are approximated by pseudo-static loads.

Micro and nano-indentation experiments have also been developed to probe mechanical parameters at smaller size scales, but the control and variable remain global in nature. To link the global response to the atomistic scale response that occurs within the material during indentation, experiments have been conducted in the SEM and TEM where slip bands and even individual dislocation events are observed in real time [1,2]. These *in situ* experiments and simulations of indentation have allowed the linking of observed discontinuities that occur during pseudo-static indentation to specific deformation events and mechanisms.

Lu *et al.* conducted an experimental investigation of strain-rate sensitivity for the indentation of oxygen-free, high conductivity copper at a velocity up to 35 m/s (which correspond to strain rates of up to 2.5 \times 10 3 s $^{-1}$) [3]. They used a 140.6 $^\circ$ cone indenter, and the indentation depth was \sim 1 mm. Both their experiments and simulations showed an increasing strain-rate dependent deviation in the load-depth response up to the maximum strain rate of their experiments. Notably, they observed stiffening and an increase in flow stress as strain rate increased. Gao *et al.*

^{*} Corresponding author at: Chandra Family Department of Electrical and Computer Engineering, The University of Texas at Austin, Austin, TX 78712, USA. E-mail address: mfbecker@austin.utexas.edu (M.F. Becker).

reported both experiments and MD simulation of the nanoindentation of single crystal Fe surfaces at a velocity of 10 m/s with a spherical nanoindenter [4]. They observed load drops in their simulated, strain-controlled force vs. displacement curves. Nanoindentation experiments and MD simulations of a 5 nm single crystal Au polyhedral nanoparticle were reported by Mordehai *et al.*[5]. The nanoindenter was a cube corner, and the load-controlled indent and withdraw cycle took place over 70 s. In the load-controlled experiments, displacement bursts were observed. When simulated using quasi-static strain control, load drops were observed that were correlated with dislocation activity.

Whereas during traditional indentation experiments a nearly rigid penetrator is indented into a deformable half-space, it is also of interest to study the behavior when a deformable penetrator contacts a deformable half space. As an example, this situation occurs when particles impact a substrate during film deposition by cold spray or micro cold spray. There has been some experimental work on understanding the global constitutive behavior when deformable particles contact substrates [6,7]. However, the strain rates that can be measured experimentally are limited to strain rates below $10^8 \ s^{-1}$, much lower than the strain rates typically experienced in micro cold spray (> $10^9 \ s^{-1}$).

The high strain rates and small particle sizes used in micro cold spray result in a very short time scale for the deformation event (<200 ps). This makes the particle impact problem difficult to study experimentally, but highly amenable to study using molecular dynamics (MD). As a result, there have been many studies that focus on the global response during nanoparticle impact and the atomistic-scale deformation mechanisms that cause that deformation [8–10]. These studies show that a range of mechanisms can arise during particle impact such as dislocation plasticity and, at higher strain rates, amorphization and viscous flow [11]. They also show that the active mechanisms depend on the particle material, impact velocity, particle size, and particle orientation [12,13].

Nanoindentation at high strain rates is of particular interest, but unfortunately there are few to no reports of experiments or MD simulations at velocities above 10^{\prime} s m/s (corresponding to strain rates greater than a few $1000~\text{s}^{-1}$). This data would provide a link between global behavior and the atomistics that drive deformation behavior during nano-contact or micro cold spray. Thus, we seek to understand the deformation mechanisms for nano-contact at higher velocities via MD simulations. We consider the response of a deformable particle when it contacts a rigid plate or the equivalent problem of a moving rigid plate contacting a deformable sphere due to the intuitive and more straightforward nature of the contact experiment.

Previous simulations of high strain rate deformation on uniform bars and nanoparticle impacts of FCC metals suggest that as strain rate increases, the deformation mechanism transitions from primarily dislocation plasticity to amorphization and viscous flow [12,14–17]. These simulations also suggest that this transition in deformation mechanism, while affected by strain rate, temperature, and particle size, can be quantitatively predicted from the potential energy per atom (PE/atom). Thus, our hypothesis for study via MD simulations is that it is possible to link the global response when a deformable particle contacts a substrate at high strain rates to specific atomistic events, such as dislocation slip, amorphization, and viscous flow. We further hypothesize that the atomistic-scale mechanisms that affect the global response of the particle can be predicted from the PE/atom.

Aluminum was selected to test these hypotheses because it is nearly elastically isotropic, exhibits an FCC structure that exhibits prototypical deformation behavior for a metal, has been studied both experimentally and in atomistic simulations, and is of practical interest. The geometry that we selected is that of a deformable sphere contacting a moving rigid plate. The chosen range of contact velocities spans from quasi-static deformation to a speed high enough for atomic disordering to dominate deformation processes (i.e., 10 to 1000 m/s).

2. Methods

Molecular dynamics simulations were conducted using the Large-scale Atomic/Molecular Massively Parallel Simulator (LAMMPS) software [18] running on the Lonestar6 high performance computer cluster at the University of Texas at Austin to study the high velocity contact of a nano-sized aluminum sphere by a rigid flat-plate. The Al99.eam.alloy embedded atom interatomic potential for aluminum [19] from the National Institute of Standards and Technology (NIST) Interatomic Potentials Repository was used due to its optimization for near-standard conditions. It gives good agreement with many parameters, including the elastic constants for aluminum and for pressure wave velocities and shapes [20].

The simulation volume is a cube 50 lattice constants (LC) on a side (for Al, LC=0.405 nm). The single crystal Al spherical indenter has a 6 nm (14.8 LC) diameter and is composed of \sim 6800 atoms). It is placed 3.24 nm (8 LC) above the simulation volume center along the z-axis at the start of the simulation. The Cartesian axes of the simulation volume are shown in Fig. 1, and the Miller indices for the Al crystal are in reference to these axes. The Al crystal lattice was oriented in one of three configurations with respect to the simulation volume and indenter surface normal: (1) with Miller indices (100), (01 $\overline{1}$), and (011) designated as [011] and shown in Fig. 1, (2) with Miller indices ($\overline{11}$ 2), (1 $\overline{1}$ 0), and (111) designated as [111], and (3) with Miller indices (100), (010), and (001), designated as [001]. The rigid plate enters from the top and moves downward with a constant velocity in the -z direction as shown in Fig. 1. The atoms within the original sphere that pass beyond the rigid plate surface are repelled with a force constant (linear spring constant) of 10 eV/Å³ (force/distance² in LAMMPS metal units). The bottom portion of the sphere up to distance z = 1.38 nm was held in place by setting each atom's momentum to zero after each time step. This held the sphere in position during the simulation, but dislocations and deformations were still allowed to propagate into this lowest region of the sphere.

Before initiating contact with moving rigid plate, the sphere was equilibrated to 300 K by a series of short 5 ps runs at 300 K using the Nose–Hoover style, non-Hamiltonian equations of motion in the isothermal-isobaric (NPT) ensemble [21] to perform the time integration with a time step of 0.001 ps (1 fs). At the beginning of each short run, the temperature of the atoms was reset to 300 K, and the equilibration was deemed completed when the temperature deviated by less than 2 K before returning nearer to 300 K. Energy conservation was then verified by using the canonical, energy conserving integrator (NVE) for 10 ps. A 1 fs timestep was found to be sufficiently small for the simulations to run accurately and conserve energy.

Contact was then initiated at the chosen velocity, and the atom positions were updated using the NVE integrator. The NVE integrator was chosen so that temperature in the closed system would not be affected by coupling to a thermal bath as would be the case if a non-conservative integrator were chosen. Displacement velocities ranged from 10 m/s to 1000 m/s. Global force and displacement data were collected every 0.001 nm for 1000 samples over the 1.0 nm of indenter motion. Contact was initiated with the sphere when the plate displaced by 0.2 to 0.4 nm, depending on the crystal orientation of the sphere. The reason for these differences between the three orientations is apparent from the contact surface atoms' positions with respect to the plate in Fig. 1. Atom positions were output every 0.02 nm for 50 frames.

OVITO (Open Visualization Tool) software [22] was used to visualize the atomic positions, and polyhedral template matching (PTM) [23] was used within OVITO to classify the local atomic configuration of each atom. The atom images were color-coded by PTM configuration, with green representing FCC and red representing HCP local atomic configuration. When the atomic configuration could not be identified (e.g., at grain boundaries, free surfaces, or where the atoms were disordered), atoms were identified as Other and were colored gray. In PTM, the RMS

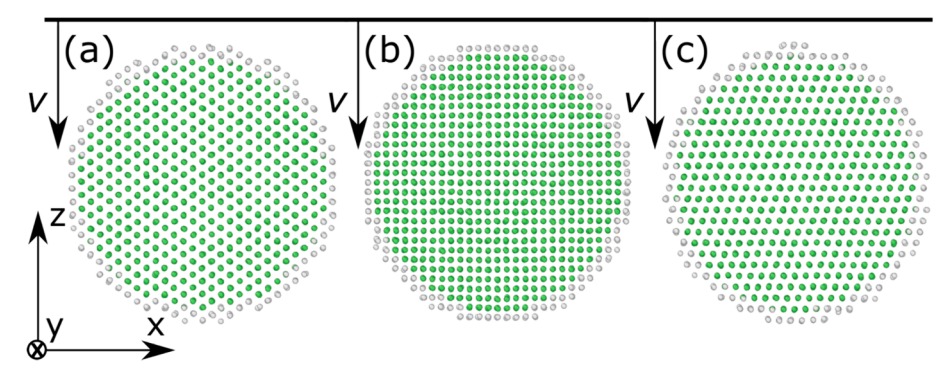


Fig. 1. Layout of the simulation with the rigid plate moving from above with velocity v in the -z direction. (a) [011] oriented 6 nm diameter sphere with Miller indices (100), (01 $\overline{1}$), and (011) viewed in the [01 $\overline{1}$] direction. (b) [001] oriented 6 nm diameter sphere with Miller indices (100), (010), and (001) viewed in the [010] direction. (c) [111] oriented 6 nm diameter sphere with Miller indices ($\overline{11}$ 2), ($\overline{11}$ 0), and (111) viewed in the [1 $\overline{1}$ 0] direction. A 1 nm thick slice through the center of the sphere is shown. Green atoms are FCC and gray atoms on the surface are Other, not identified by PTM. The cartesian axes of the simulation volume are shown at the left, and the Miller indices are referenced to these axes.

deviation cutoff was set to 0.15, which was within the guidelines for distinguishing between distorted or disordered crystals. Dislocation types were identified by dislocation analysis (DXA) [24] in OVITO, and their lengths were summed to determine the total dislocation length. LAMMPS also output potential energy per atom (PE/atom) and kinetic energy per atom (proportional to temperature). For computing histograms, OVITO compiled PTM configuration and PE/atom for the 6800 atoms. One global variable that is of particular interest is total energy, which was differentiated with respect to displacement to give the contact force. Thus, contact displacement was the global control variable and contact force was the global measured variable in the simulations.

Simulations were conducted for the three crystal orientations noted above and for contact velocities of 10, 20, 50, 100, 200, 500, and 1000 m/s. Time integration used the canonical, energy conserving integrator (NVE). Displacement of the sphere ended after 1.0 nm of travel of the plate. An individual force vs. displacement curve was generated for each simulation and further analyzed to determine the participation of individual atoms in the various deformation mechanisms.

When analyzing the atomic-scale behavior during contact, it is useful to know the microscopic strain rate associated with each contact velocity. By analyzing per atom behavior, the displacement velocity is correlated with the maximum strain rate per atom within the sphere just below the plate. First, strain is plotted versus increasing displacement, and thus increasing time, by averaging the atomic strain per atom for each successive output frame of atom positions for a group of ~ 10 randomly selected atoms in the 3rd and 4th atomic layers in the sphere just below the contact surface. The maximum slope of this curve is taken as the maximum strain rate. Eliminating those atoms near the contact surface and the free surface of the sphere eliminates strain artifacts. We find that strain rate scales linearly with displacement velocity within one digit accuracy, as shown in Table 1.

3. Results

Results are presented for global force vs. displacement. Since load drops and plasticity are observed in the force vs. displacement curves, the simulations are examined at the atomic level to show the fraction of

Table 1Maximum nominal strain rate for atoms in the sphere just beneath the contact surface for different contact velocities.

Velocity (m/s)	Max strain rate (s ⁻¹)	
1	8 × 10 ⁸	
10	8×10^9	
100	$8 imes 10^{10}$	
1000	$8 imes 10^{11}$	

atoms that contribute to each deformation mechanism. Cross section views of the spheres are shown that illustrate the various deformation mechanisms. Shockley partial dislocations have been shown to be the prevalent dislocations during deformation a moderately high strain rates in other FCC crystals [25,26]. The passage of a Shockley partial dislocation in an FCC crystal results in an HCP stacking fault, and thus, partial dislocations are characterized via atoms in the HCP configuration. Amorphization is studied by counting the number of atoms that become disordered. Since PE/atom has been shown to predict the onset of disordering of metal crystals at high strain rates in MD simulations, [12,16] its influence is examined through PE/atom histograms and further by histograms where the atoms are grouped by their PTM classification.

3.1. Force vs. Displacement

The results for force versus displacement simulations are presented in Fig. 2. Total energy values are output at displacements of every 0.001 nm and differentiated with respect to depth to derive the indenter force. A 9-point moving average is applied to smooth oscillations in the force that have a period 60–90 fs that are present in the total energy. This level of smoothing is selected because it preserves larger scale fluctuations while smoothing the noise that is endemic to MD simulations of this nature.

At low velocities (10–200 m/s), the curves have initial rises corresponding to elastic deformation that ends with a distinct load drop with the nucleation of the first dislocations. The elastic segments of the curves all lie on top of one another up to 100–200 m/s. Beyond this point, the response begins to stiffen for higher velocities in much the same way as observed by Lu *et al.* [3] Larger displacements beyond the first load drop result in a more complex plasticity behavior comprised of sequential load drops. The magnitudes of the load drops decrease as velocity increases, and they become even less distinct as velocity increases to 100 m/s.

Immediately apparent from Fig. 2 is the transition in behavior between velocities of 100 and 200 m/s, where several characteristics of the force vs. displacement curves change. The force drops become force plateaus at 100 m/s and disappear by 500 m/s. At the highest velocities, stiffness increases even more dramatically. In this range, two distinct behaviors are observed: rises and plateaus in force are associated with the incorporation of additional atom layers participating in deformation as the contact area increases, and oscillations occur that are attributed to energy fluctuations inherent to the LAMMPS simulation, as previously noted. In the former case, the plateaus are barely discernable for the [011]-oriented sphere, but they are more prominent in the [111] orientation and even more so in the [001] orientation. Determining the sources of the global plasticity observed in the plots shown in Fig. 2

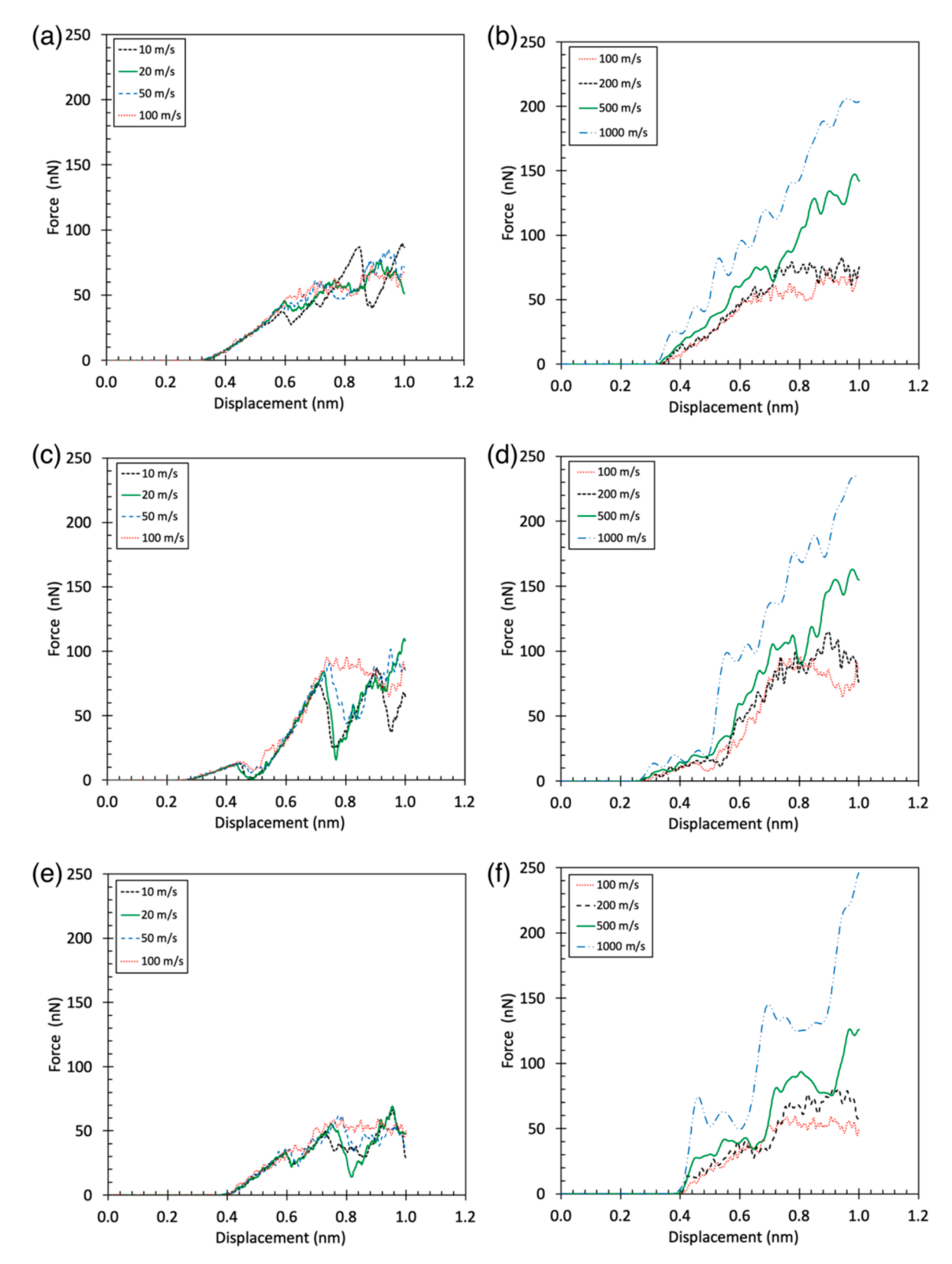


Fig. 2. Force vs. displacement plots for impact of rigid plates onto deformable indenters with orientations [011] in (a)-(b), [111] in (c)-(d), and [001] in (e)-(f). Low velocity plots are on the left (10–100 m/s), and high velocity plots are on the right (100–1000 m/s). The 100 m/s curve is duplicated on the left and right plots to facilitate comparisons.

requires atomic-scale investigations that are analyzed in the sections that follow.

3.2. PTM structure classification and total dislocation length

Since dislocations play an important role in deformation during contact, we begin by analyzing the crystal structure of atoms by PTM analysis and the total dislocation length as a function of displacement. Note that total dislocation length is proportional to dislocation density for the fixed volume of the simulation atoms. PTM analysis also identifies atoms that become disordered and are classified as Other because they cannot be identified as a known crystal structure. Tracking these disordered atoms is important since disordered atoms can contribute significantly to plasticity via viscous flow. Dislocations are counted in each dumped image (every 0.02 nm in displacement) up through the third load drop for [011] orientation and the second load drop for the other two orientations. Because dislocations in all images are summed, a moving dislocation may be counted several times in successive images.

One hundred dislocations were counted, with 65 being Shockley dislocations. Uniquely for the [001] orientation, 29 were Hirth dislocations formed by the intersection of four Shockley dislocations into a relatively stable lock structure. Thus, 94 % of the dislocations were Shockley or derived from the locking of Shockley partial dislocations. Since the region between the lead and trailing Shockley partials produce an HCP stacking fault in FCC crystals, atoms classified as HCP in stacking faults are likely associated with these dislocations. This strong correlation is quantified by the following statistical analysis.

For all velocities up to 100 m/s and for all displacements, a regression analysis was performed for each crystal orientation. Over 170 observations were analyzed where the dislocation length was nonzero, and the velocity was \leq 100 m/s. Heating and subsequent annealing and/or disordering occurs at higher impact velocities which results in a drop in dislocation length that is more rapid than the increase in the number of HCP atoms for large displacements. Thus, cases above 100 m/s were not included in the regression analysis. For the [011], [001], and [111] crystal orientations, analysis of variance gave correlation coefficients

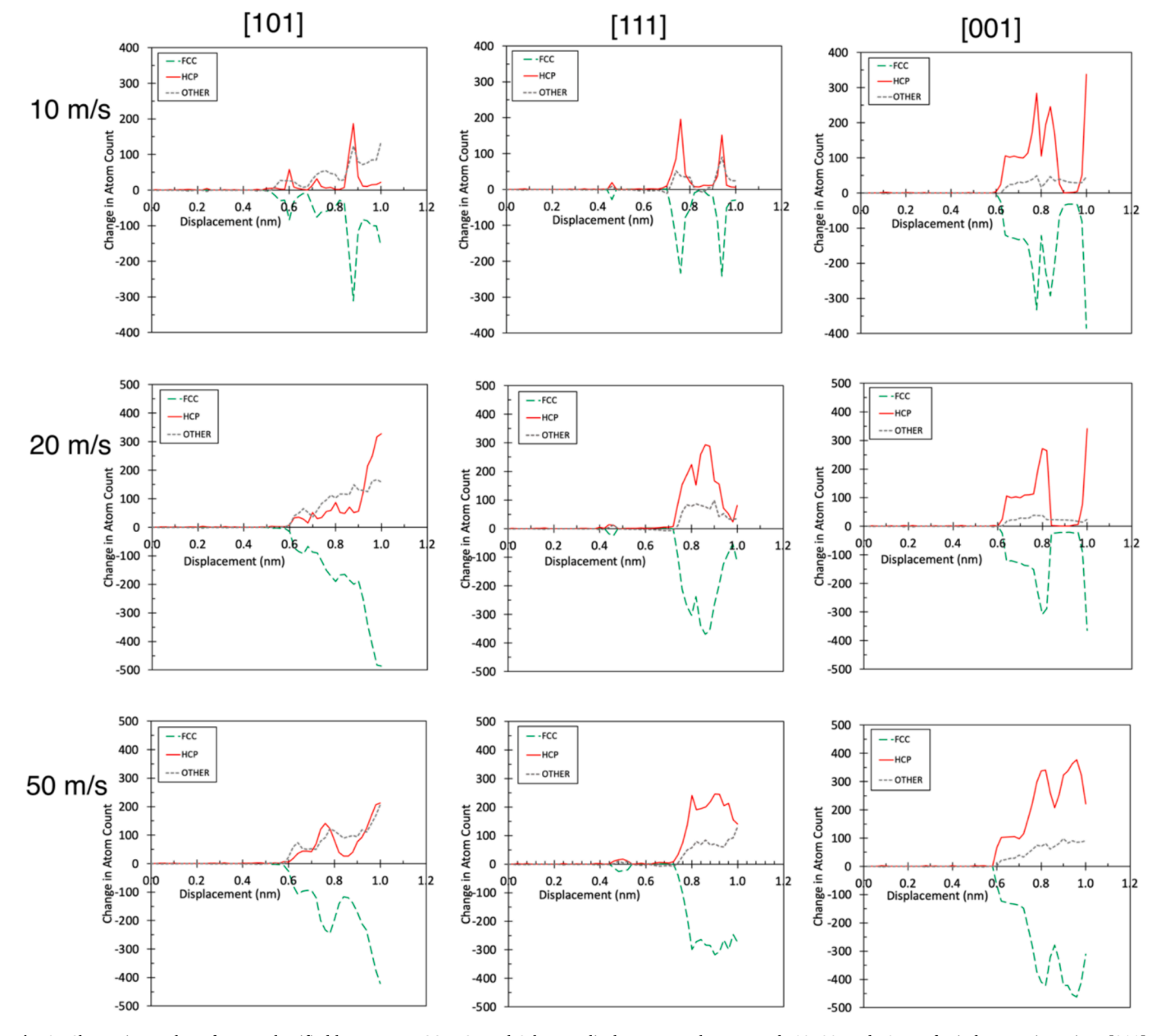


Fig. 3. Change in number of atoms classified by PTM as FCC, HCP and Other vs. displacement at lower speeds 10, 20, and 50 m/s for indenter orientations [011], [111], and [001].

between change in HCP atom numbers and total dislocation length that were 0.92, 0.94, and 0.96, respectively. Thus, 85 %, 88 %, and 92 % of the increase in the number of HCP atoms can be attributed to the increase in the total dislocation length. This analysis confirms that the

behavior of the total dislocation length versus displacement mirrors the HCP atom numbers versus displacement. Although closely correlated, HCP atom numbers and total dislocation length contain slightly different information when viewed over time. A stacking fault containing HCP

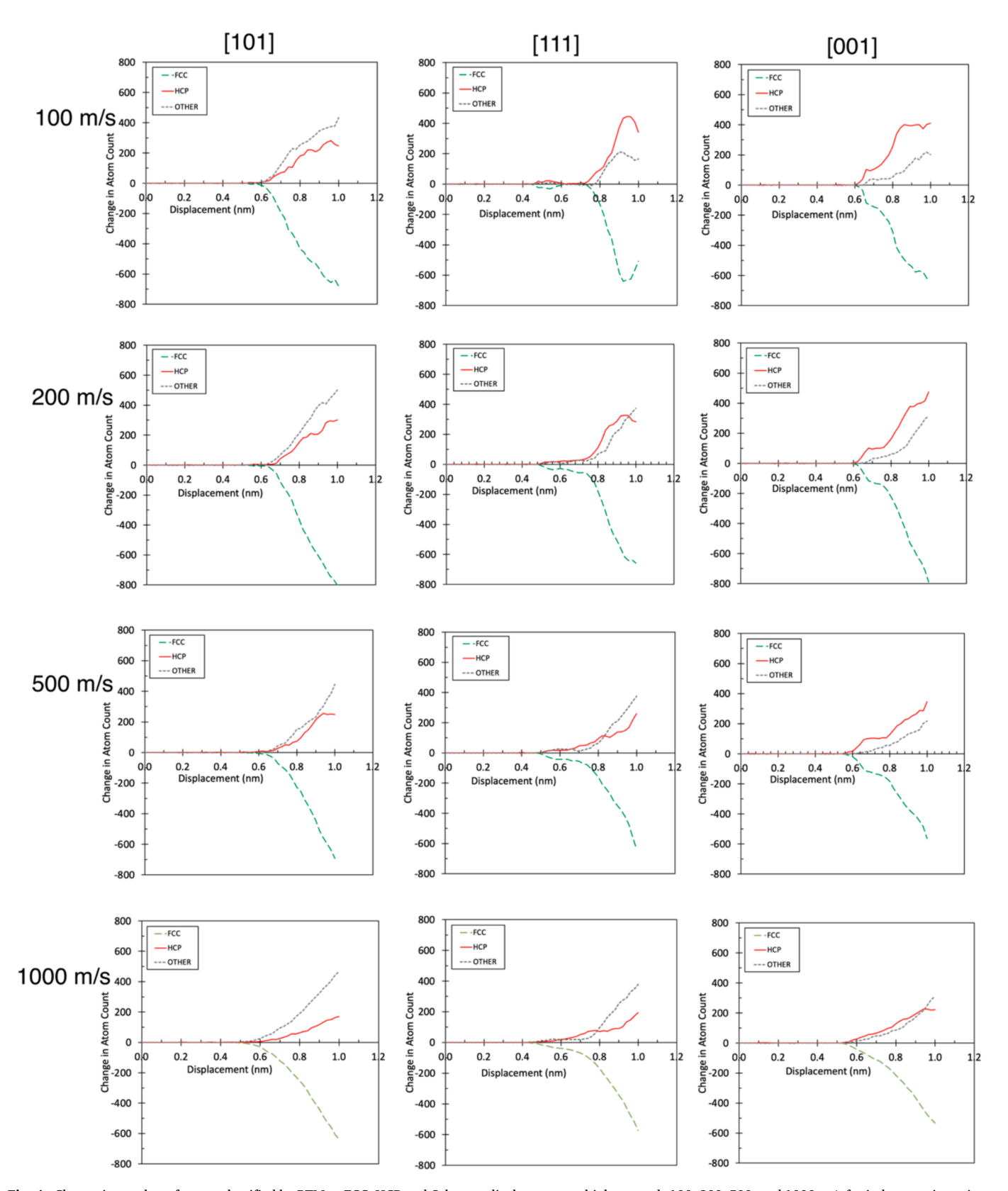


Fig. 4. Change in number of atoms classified by PTM as FCC, HCP and Other vs. displacement at higher speeds 100, 200, 500, and 1000 m/s for indenter orientations [011], [111], and [001].

atoms can persist after a dislocation disappears; therefore, HCP atom numbers give a better accounting of cumulative dislocation plasticity. Accordingly, we plot number of HCP atoms rather than the total dislocation length in Figs. 3 and 4.

Figs. 3 and 4 show the change in atomic classification numbers versus displacement for all cases. The initial elastic rise in the force--displacement curve for all orientations is characterized by stable atomic configurations (i.e., few atoms transforming away from their initial FCC configuration). This region extends up to a displacement of 0.6 nm for the [011] and [001] orientations and up to 0.46 nm for the [111] orientation. Marked by the first load drop, the onset of plasticity is accompanied by increased numbers of HCP and Other atoms and the appearance of Shockley dislocations. At low velocities (100 m/s and below), there is no significant heating from dissipative plastic deformation processes; nevertheless, Fig. 3 shows that in situ annealing occurs by the decrease of HCP and Other atom numbers and correspondingly, a reduction in dislocation length [27]. The mechanisms for defect reduction are observed to be both the retreat and/or annealing of defects and the propagation of trailing Shockley dislocations to a surface to become perfect dislocations. This is particularly pronounced for the [111] orientation where the defects disappear over a large range of displacements (0.48 to 0.70 nm), and the force goes to zero before rising again in another prolonged elastic segment. Defects are not nucleated again until the second load drop is reached at a displacement of 0.70 nm. Similar behavior is repeated for velocities of 10-50 m/s, although the load drops become smaller and less sharp as velocity increases.

Load drops are also associated with the increase in the total dislocation length, followed immediately by a decrease in total dislocation length that mirrors the behavior of the number of HCP atoms. Coincident with dislocation plasticity, some amorphization is occurring as indicated by the increase in Other atom numbers. As velocity increases from 200 to $1000 \, \text{m/s}$, the number of Other atoms eventually overtakes the number of HCP atoms.

The most notable difference in the evolution of crystalline structure for spheres with different crystal orientations at low velocities is the large load drop for the [111] orientation back to zero force before increasing again up to the next load drop, whereas the other orientations show generally smaller load drops. The atomic behavior associated with the load drops and with their disappearance at higher velocities will be addressed next in the atomic scale analysis of the simulation results and in the Discussion section.

3.3. PTM classification and dislocation length versus velocity

To better illustrate the changes in deformation behavior as velocity increases for the different crystal orientations, the data in Figs. 3 and 4 are summarized in Fig. 5 by plotting the maximum change in HCP and

Other atom numbers and the maximum total dislocation length versus velocity for the three orientations. These plots clearly show that as velocity increases, there is a crossover betewen decreasing HCP atom numbers (and decreasing total dislocation length) and increasing numbers of disordered atoms. Note that dislocation activity is correlated with increases in the HCP atom numbers and total dislocation length, and that viscous flow is correlated with the number of disordered atoms. This crossover is not seen at the same velocity for each orientation. The crossover occurs at the lowest velocity for the [011] orientation, somewhat higher for the [111] orientation, and at the largest velocity for the [001] orientation. This tradeoff between HCP and disordered atoms also indicates a changeover between the deformation mechanisms of dislocation-driven plasticity and viscous flow as velocity is increased. At the highest velocities, the increasing stiffness observed in the force vs. displacement curves (Fig. 2) is accompanied by a decreasing fraction of atoms participating in the deformation mechanisms. Note that for velocities greater than 200 m/s, both the peak number of HCP atoms and the maximum dislocation length are decreasing as velocity increases. For the same velocity range, the number of disordered atoms reaches a plateau. The cause of this behavior will be examined in the discussion

The simultaneous decrease in dislocation activity at velocities above 200 m/s and the plateau in the number of Other atoms might be somewhat surprising were it not for annealing. The maximum temperature attained by a significant number of atoms is indicated in Table 2. Heating to above 1200 K is observed at 1000 m/s; and much smaller, but still significant, heating is observed at 500 m/s, which can enable thermally assisted annealing of defects and amorphous atoms. However, in all cases, the temperature peak is very transient, lasting less than 0.2 ps, and it is localized within volumes less than a few cubic nanometers. There are two relevant consequences to the very short and localized nature of the heating: 1) The effects of heating are reduced compared to isothermal temperature increases that are typically applied in laboratory studies. 2) Even when the temperature briefly exceeds the thermodynamic melting temperature in small volumes, there is likely insufficient time to allow melting followed by resolidification.

Table 2Maximum observed temperature versus displacement velocity for the three sphere orientations. The initial sphere temperature is 300 K.

Displacement Velocity (m/s)	Maximum Temperature (K) Crystal Orientation		
	1000	>1200	>1200
500	< 600	< 700	< 700
200	< 500	< 600	<450

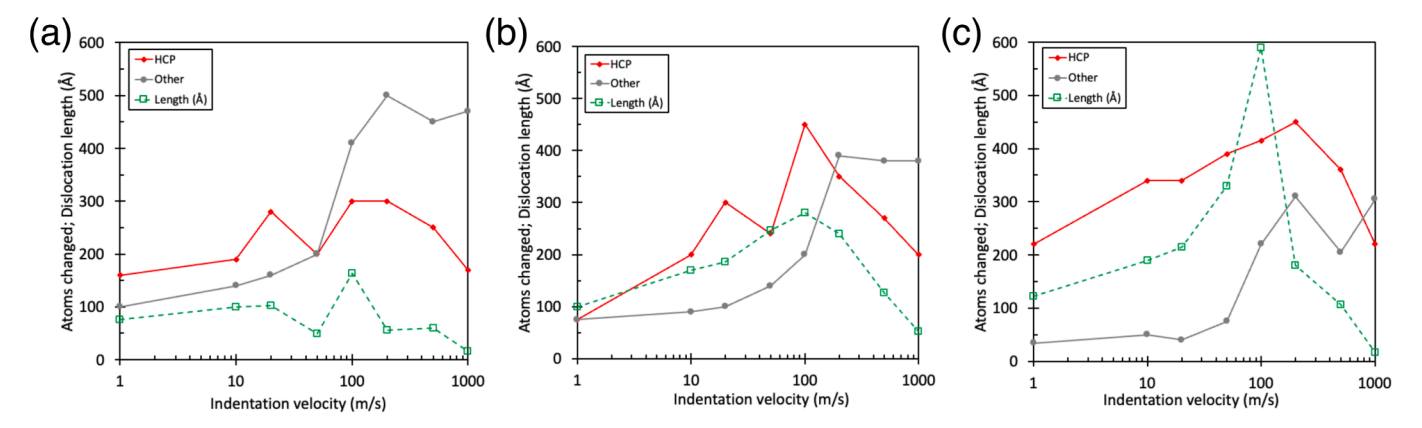


Fig. 5. Summary plots of maximum number of atoms changed to HCP and Other, and maximum total dislocation length (Å) vs. velocity for sphere orientations: (a) [011], (b) [111], and (c) [001].

3.4. Examples of deformation morphologies for slow and fast displacement velocities

3.4.1. Slow displacement velocities - Dislocations dominate

For contact at 20 m/s, dislocations dominate the deformation process. The number of atoms with an HCP configuration is considerably larger than the number of Other atoms, and they are at a local maximum as shown in Fig. 5. The majority of defects identified by DXA analysis are Shockley dislocations, which are constrained to lie in {111} slip planes. The crystal orientation of the Al sphere determines how deeply these slip planes penetrate. For example, Fig. 6a shows a [011]-orientated sphere in which the {111} planes lie at a relatively shallow angle. Thus, the dislocations (shown as lines of red atoms) are unable to penetrate very deeply. On the other hand, Fig. 6 b–d show [111]- and [001]-oriented spheres, where the {111} planes lie at steeper angles, and the defects can penetrate through the entire sphere. Fig. 6 c & d show successive atom images of a [001]-oriented sphere separated by 1 ps in time (equivalent to 0.02 nm in displacement) in which the visible dislocation continues to move deeper into the indenter, as indicated by the arrow.

Excluding surface atoms, there are relatively few disordered atoms classified as Other (shown by the gray atoms in Fig. 6) at slow displacement velocities. They are most numerous for the [011] orientation where they are visible within the sphere and near the contact surface in Fig. 6a. For the [011] orientation, disordering and viscous flow occurs because this orientation is unfavorable for accommodating the required strain by dislocation penetration. For the other two orientations with a larger number of HCP atoms and deeper dislocation penetration, the number of disordered atoms is correspondingly smaller.

3.4.2. Fast displacement velocities - Disordered atoms dominate

For contact at 200 m/s, the number of disordered atoms peaks, as shown in Fig. 5. An immediate observation is that the number and total length of dislocations has grown as compared to the lower velocities (see Fig. 5), however the individual dislocation lengths are considerably shorter because the high displacement velocities produce local strain rates beneath the plate $> 10^{11} \ {\rm s}^{-1}$. At such high strain rates, there is insufficient time for long dislocations to propagate as compared to slower velocities at the same displacement.

Fig. 7 illustrates views of spheres with [011] and [001] orientations contacted at 200 m/s, which have the most and fewest disordered atoms, respectively. The corresponding lack of defects and HCP atoms is clearly visible in the [011] case. The [001] case has relatively more HCP atoms and defects, but they have not penetrated nearly as far as they did at a velocity of 20 m/s at a smaller displacement in Fig. 6d. Also notable in Fig. 7a is the wider contact patch for the [011] case. Only the region just beneath the plate is defected and disordered, so the atoms have had to displace laterally to accommodate the contact deformation. Since most of these at atoms are disordered, the deformation mechanism is viscous flow.

3.5. Evolution of histograms of PE/atom

An indicator that atoms are likely to disorder in MD simulations of metals strained at sufficiently high rates is that the potential energy per atom (PE/atom) excedes a threshold value that can be determined in advance by knowing the PE/atom at the melting point of the material. This criterion has been found to apply to silver and gold subjected to uniform uniaxial [16] and biaxial strain [17] and for the impact of spherical silver particles onto planar silver surfaces [12]. To see if

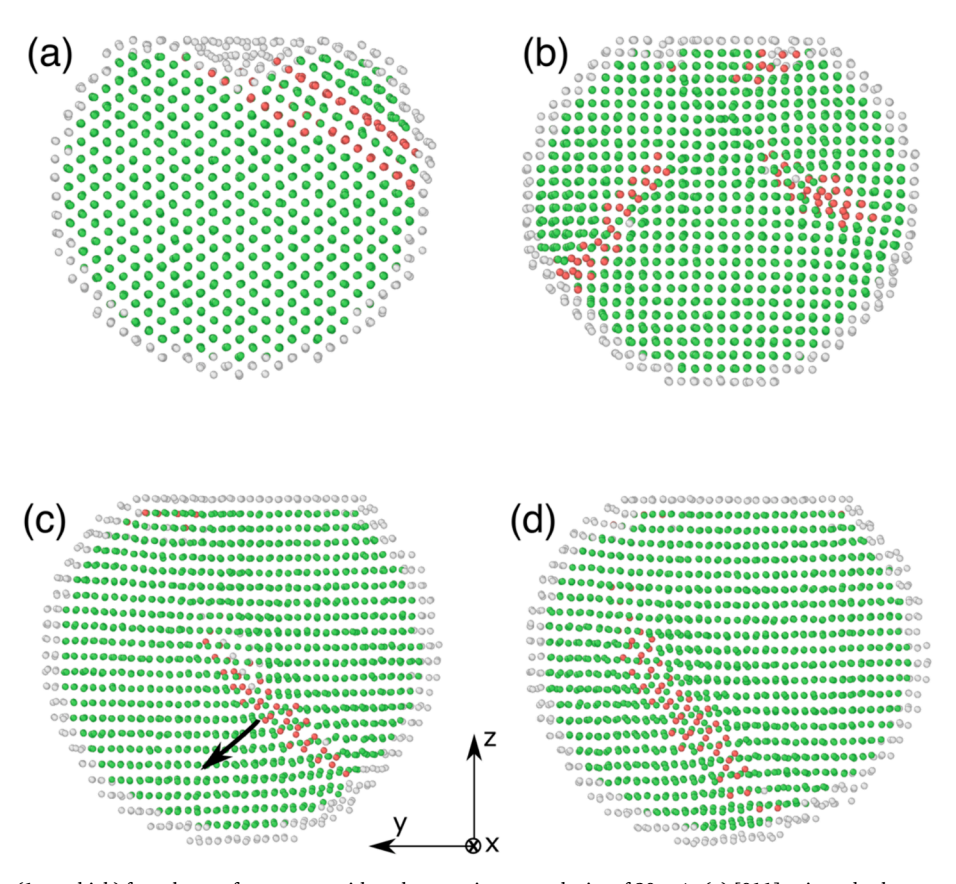
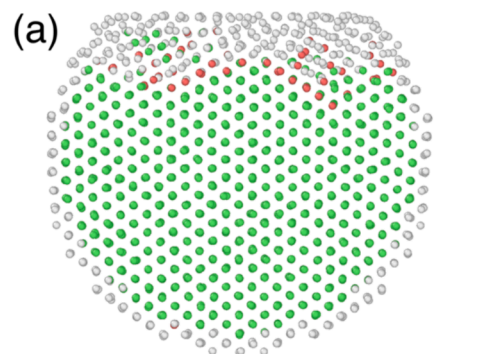


Fig. 6. Cross section views (1 nm thick) for spheres after contact with a plate moving at a velocity of 20 m/s. (a) [011]-oriented sphere at a displacement of 0.96 nm. (b) [001]-orientated sphere at a displacement of 0.80 nm. (c) and (d) are a [111]-oriented sphere at displacements of 0.90 and 0.92 nm, respectively, that shows dislocation motion over a time interval of 1 ps. The arrow in (c) indicates the motion direction of the dislocation. The reference axes of the simulation box are shown between (c) and (d), and the crystal orientations are as given in Fig. 1 referenced to these axes.



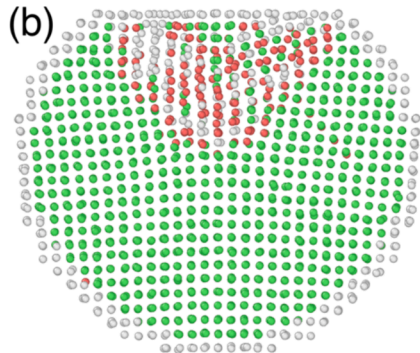


Fig. 7. Cross section views (1 nm thick) of spheres at a 200 m/s contact velocity. (a) [011]-oriented sphere indented to a displacement of 1.00 nm. (b) [001]-oriented sphere indented to 1.00 nm.

disordering follows the same rule for the contact of Al spheres, we look at the evolution of histograms of PE/atom during contact and further divide the histograms by their PTM crystal classification.

First, the critical PE/atom is determined indepenently by measuring the PE/atom in aluminum just below its abrupt rise when the metal melts. For the Al.99.eam potential used in these simulations, the melting transition was simulated by heating a uniform, 20 nm on-a-side cube of single crystal Al and plotting the average PE/atom from all of the non-surface atoms [16]. The critical PE/atom at the initiation of the melting transition is $-3.202~{\rm eV}$. For reference, the average value of PE/atom at 300 K is $-3.311~{\rm eV}$.

The histograms are constructed after first excluding the surface atoms because they have anomalously high PE/atom. These atoms are identified by having a coordination number < 10 (out of 12 for an FCC metal). Once these atoms are excluded, all the atoms initially have PE/

atom of less than -3.00 eV at 300 K, but there is a range of PE/atom at finite temperatures because of thermal fluctuations. Atoms in the second subsurface layer are still mostly classified as Other, but have PE/atom of -3.00 eV or lower. These atoms remain in the histograms, and are visible in Fig. 8 a & d in the range of PE from -3.20 to -3.00 eV. Fig. 8 a & d also show the initial state of the sphere at 300 K, and they are the identical for all crystal orientations.

Once contact has intitiated, histograms are presented in two formats. The top row (Fig. 8a–c) contains histograms of all atoms (in blue) accompanied by the change between the count at the indicated displacement and the initial PE/atom (in orange). The bottom row (Fig. 8d–f) contains histograms of all the atoms divided into the three classifications of FCC, HCP and Other (denoted as green, red, and gray respectively).

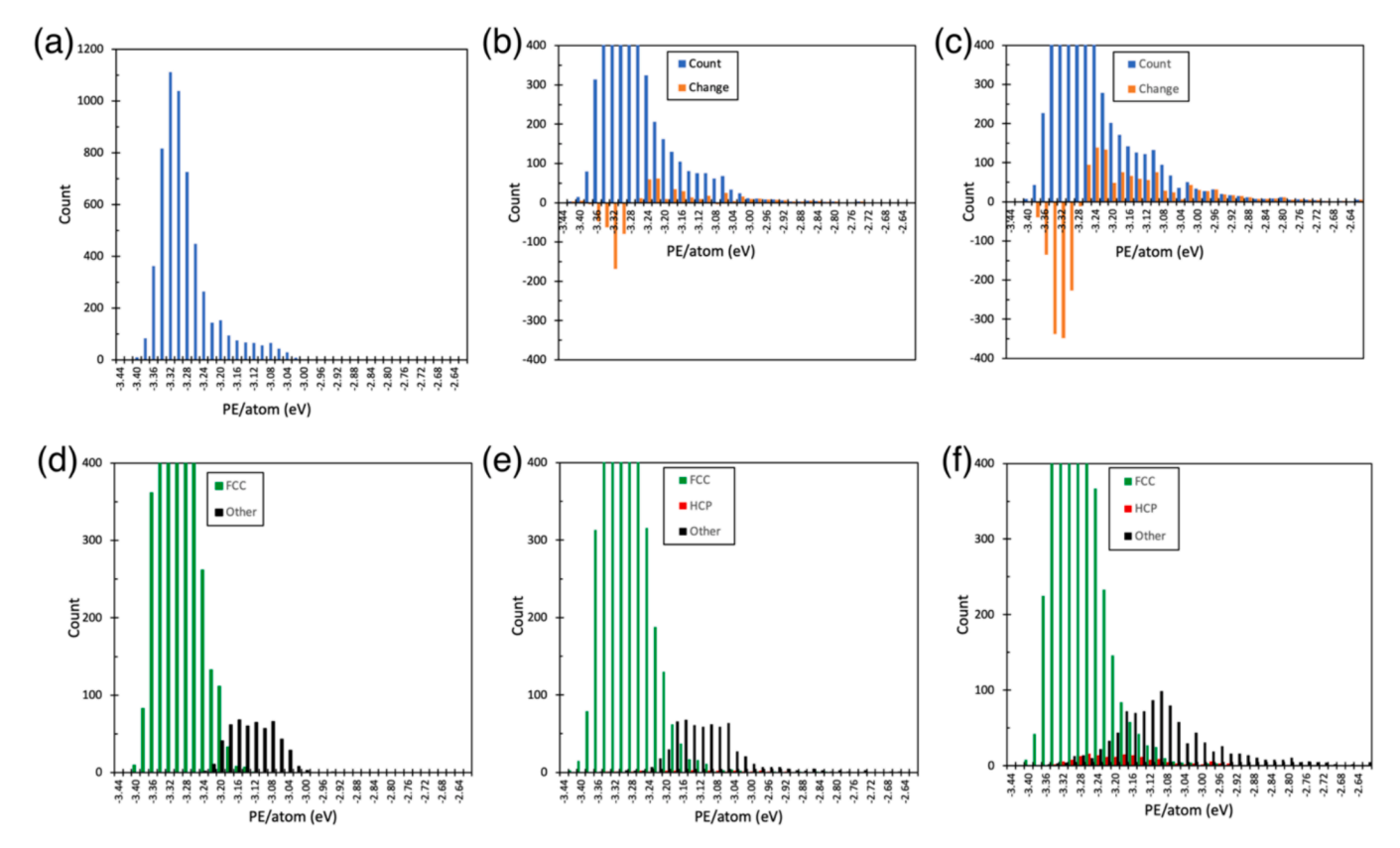


Fig. 8. Histograms of PE/atom for a velocity of 1000 m/s for a [011]-oriented sphere: (a) before contact and (d) before contact sorted by PTM classification. Histograms of PE/atom and the change compared to no contact at displacements of (b) 0.7 nm and (c) 1.0 nm. Histograms sorted by PTM classification at displacements of (e) 0.7 nm and (f) 1.0 nm. Note that the vertical scale in (b)–(f) is expanded so that the peak is off scale and thus appears truncated.

3.5.1. [011] orientation at 1000 m/s (largest number of disordered atoms)

First, we examine histograms for the case with the largest number of disordered atoms, the [011] orientation contacted at 1000 m/s. In Fig. 8 b & c, atoms depart from the lower side of the energy distribution centered around -3.32 eV and are added over a wide range of energies on the higher energy side of the distribution. Some of these changed atoms end up at energies above -3.00 eV. As expected, the number of atoms making the transition to higher PE/atom increases as displacement increases from 0.7 to 1.0 nm. Further granularity is added by examining the PTM configuration histograms in Fig. 8 d–f where the number of HCP atoms increases with defect motion, and they peak broadly around -3.20 eV at the largest displacement. The smaller number of HCP atoms at 0.7 nm displacement are not visible on the graph, but they have a similar broad energy distribution, and their numbers are about 1/8 of that at a displacement of 1.0 nm.

Preserved across Fig. 8 d–f, is the division between FCC and Other atoms that occurs at -3.20 eV, which lies between their respective histogram peaks. As displacement increases, atoms are added at higher energies, with the majority of those exceeding -3.20 eV becoming disordered. The HCP atoms lie in an energy range centered between and overlapping the distributions of FCC and Other atoms with virtually

none of them having PE/atom greater than $-3.00\,\text{eV}$. On the other hand, many of the new Other atoms have PE/atom values greater than $-3.00\,\text{eV}$.

3.5.2. [111] orientation, 20 m/s compared to 1000 m/s (change in deformation mechanism)

The [111] orientation is midway between the other two orientations with respect to its degree of changeover from dislocation-dominated plasticity to plasticity dominated by viscous flow of disordered atoms. As shown in Fig. 5b at 20 m/s, defect activity is largest (largest number of HCP atoms); and at 1000 m/s, disordered atom numbers are high and HCP atom numbers have decreased from their peak at a lower velocity. Fig. 9 shows histograms for the [111] orientation at 1.0 nm displacement that further illustrate this changeover in deformation mechanism.

For a displacement velocity of 20 m/s, Fig. 9a shows most of the changed atoms going to energy states below -3.20 eV. Fig. 9b shows significantly more atoms arriving at energies greater than -3.20 eV for a displacement velocity of 1000 m/s. Fig. 9d reveals that these highenergy atoms are classified as Other and thus are disordered. Comparing the initial, pre-contact histogram in Fig. 8d with Fig. 9c at a 20 m/s velocity and 1.0 nm displacement, there is a small change in

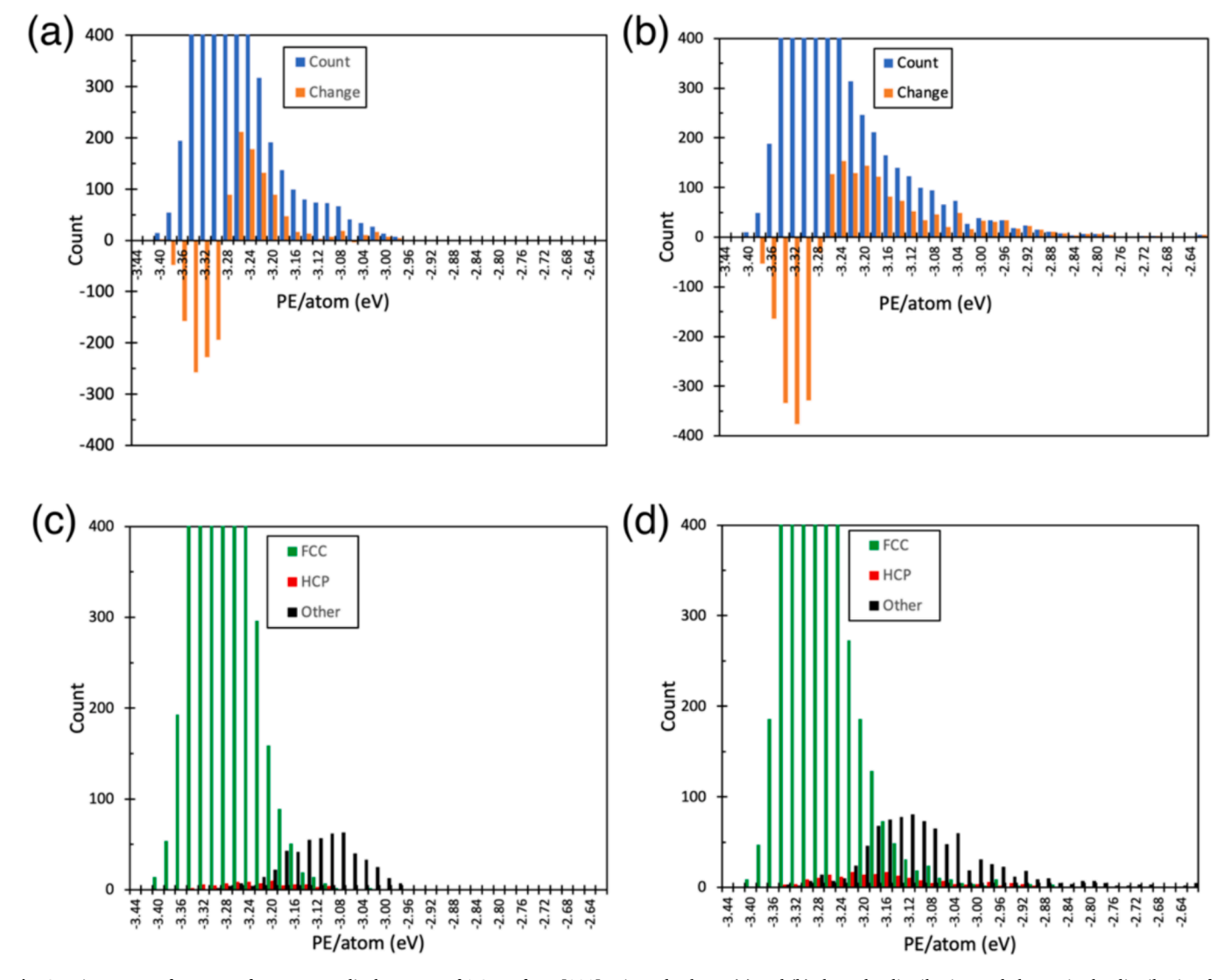


Fig. 9. Histograms of PE/atom for a contact displacement of 1.0 nm for a [111]-oriented sphere: (a) and (b) show the distribution and change in the distribution for velocities of 20 m/s and 1000 m/s, respectively. Histograms sorted by PTM classification are shown in (c) and (d) at velocities of 20 m/s and 1000 m/s. Note that the vertical scale in all the histograms is expanded so that the peak is off scale and thus appears truncated.

Other atom numbers as well as the presence of HCP atoms in the latter plot. The high energy end of the Other atoms' distribution is not significantly changed.

At a velocity of 1000 m/s, the situation is different, and the largest shift in atom classification is from FCC to Other at energies greater than -3.20 eV, as seen by the extended high-energy tail for the Other atoms in Fig. 9d. Although the number of HCP atoms is greater at 1000 m/s compared to 20 m/s, they still reside in the same energy range centered between the FCC and Other atoms.

4. Discussion

The results presented here clearly show the existence of the transition in deformation behavior as displacement velocity increases as we hypothesized. At low velocities, the expected defect-dominated plasticity is observed. Dislocation nucleation and propagation is clearly evident in the load drops in the force vs. displacement curves in Fig. 2. These observations agree with previous nanoindentation experiments and simulations at low indentation velocities [4,5] and serve to validate our methodology.

Atomistic diagnostics confirm that the initiation of dislocation activity is correlated with the load drops. In particular, both the dislocation lengths (of mostly Shockley dislocations) and the number of HCP atoms that have transitioned from FCC give a quantitative measure of dislocation activity. As displacement progresses, the minima of successive load drops are associated with spontaneous annealing of the defects that initiated at the start of the drop. After the drop, the count of HCP atoms decreases, sometimes to zero, yet the local temperature is still near 300 K.

As displacement velocity increases above 100 m/s, the force vs. displacement curves show that the magnitudes of the load drops are reduced and eventually disappear. Coincident with these changes in the global displacement behavior as velocity increases is the simultaneous increase in the number of disordered atoms as shown in Figs. 3-5. Since we hypothesize a threshold PE/atom for amorphization, we introduced histograms of PE/atom to show that atoms that amorphized have PE/ atom values above the threshold. Figs. 8 and 9 show the bifurcation in energy distribution between disordered (Other) atoms and FCC atoms. The critical energy for amorphization is found to lie between the mean energies for the FCC and disordered atom distributions. Past simulations have shown that the transition to disorder is not an immediate switch in state, but for individual atoms the transition can occur with a variable time delay after the threshold PE/atom is reached [16]. If the strain state of the atoms is nonuniform, the fluctuation of an atom's state between FCC and disordered is correlated with fluctuations in the PE/atom [12]. Hence, the spread in energies of the FCC and disordered distributions (in Figs. 8 & 9) are not unexpected. Finally, the HCP atoms associated with dislocation activity are found at intermediate energies overlapping both the FCC and disordered atoms.

As shown in Figs. 2-5, the annealing of HCP and disordered atoms that is observed at the end of the load drops at low displacement velocity continues at higher velocities. At the highest velocities of 500 and 1000 m/s, the annealing rate is accelerated by the local temperature rise (see Table 2). This increased annealing rate results in the number of both HCP and disordered atoms peaking at around a velocity of 200 m/s and then decreasing as displacement velocity continues to increase.

As displacement increases from 0.7 to 1.0 nm, the increased disordering of atoms at higher PE/atom is shown in the representative histograms in Fig. 8 for displacement at 1000 m/s. The large number of disordered atoms present at higher velocities facilitate plastic deformation of the sphere via viscous flow. This is particularly visible in Fig. 7a for a [011]-oriented sphere indented at 200 m/s. The deformation is localized in a layer of disordered atoms near the contact surface. No dislocations are seen propagating into the interior of the sphere.

The conclusion that we draw from these data is that at higher displacement velocities, dislocation activity becomes insufficient to accommodate the applied strain. Consequently, the PE/atom increases and exceeds the threshold for disordering. At this point, viscous flow of disordered atoms accommodates further deformation. This transition in deformation mechanisms becomes broadened as it becomes spread over a group of atoms experiencing a range of strains, strain states, and strain rates.

It is important to distinguish between changes in the number of atoms that have a given atomic configuration (FCC, HCP, or Other) and their potential contributions to the global strain experienced within the sphere. The elastic limit defines an upper bound to the strain that can be accommodated by atoms in the FCC configuration. A group of atoms that experience strain larger than this limit must relieve that strain through a change in configuration. This can be accomplished either by nucleating a dislocation or through amorphization of some of the atoms in this group. Subsequent strain can be accommodated via plastic deformation without a further change in the number of atoms in each configuration by either dislocation propagation or by viscous deformation. Conversely, additional strain can also be accommodated through a further change in the number of atoms in each configuration by either nucleating additional dislocations or by amorphizing a larger fraction of atoms in the group so that additional viscous deformation occurs. Thus, neither the number of atoms that are in in each atomic configuration nor the total dislocation length (proportional to dislocation density) provides direct information about each atom's contribution to the global strain. However, these diagnostics can identify locations within the sphere where the strains and strain rates are sufficiently large to initiate plastic deformation as well as the mechanisms responsible for that deformation.

Crystal orientation is found to affect the deformation behavior of the Al spheres. Initially, the orientations of the {111} slip planes influence the location of Shockley dislocations and numbers of HCP atoms associated therewith. This is particularly true at lower displacement velocities where the dislocation activity shows a strong resemblance, both in global morphology and in the specific role played by Shockley dislocations on favorably oriented {111} planes, to the initial deformation behavior of the impact of similarly sized Ag nanoparticles on planar Ag surfaces [13]. Final aspect ratios of the deformed Ag spheres were found to increase (i.e., increasing deformation) going from [011] to [111] to [001] nanoparticle orientations. The present work differs in that the impact surface is now a rigid plane; however, the plastic deformations of the spherical indenters are analogous. Thus, we have shown how changes in atomic configuration correlate with changes in the global response as crystal orientation is varied.

As displacement velocity increases, larger numbers of atoms amorphize near the contact surface and in proximity to the dislocations. Thus, HCP atom numbers increase going from [011] to [111] to [001] orientation due to more favorable {111} plane orientations for the latter orientations, while disordered atom numbers have the opposite behavior. Overall, the number of disordered atoms increases with displacement velocity (see Figs. 3 and 4), but the differences in the number and fraction of HCP and Other atoms with crystal orientations that were present at low velocities persist even at very high velocities. The differences in the number and fraction of HCP and Other atoms between orientations also persist from the early to the latter stages of contact for a given velocity.

Direct amorphization without first initiating dislocation activity is not observed, which suggests that dislocation activity is necessary to achieve disordering. The final global shape and the atomic configurations are dependent on details of this initial dislocation activity. Even when the dislocations have been annealed or replaced by disordered atoms in the final state, the observed disordering is a direct result of the original dislocation activity.

5. Conclusions

For the deformation of spherical FCC aluminum spheres contacted by a rigid plane, the data presented here have confirmed our hypothesis that the details of the global response to nanoindentation are directly correlated with the atomistic events of dislocation slip, amorphization, and viscous flow. At low displacement velocities, the expected dislocation-driven plasticity is observed. At high indentation velocity (and consequently high strain rates), these simulations confirm a changeover from dislocation plasticity to disordering and viscous flow. This behavior was predicted and subsequently observed at high strain rates. The changeover for high displacement velocity is manifested in both the global response of the force versus displacement curves and in changes in atomic classifications as well as dislocation behavior. Interestingly, the dislocation-dominated deformation that occurs during the initial stages of deformation even at high displacement velocities plays an important role in determining the final shape even when the original dislocations and previously disordered atoms have annealed. The path dependence in the deformation persists, but it is found to differ for each unique crystal orientation of the spheres.

In MD simulations, PE/atom is an accessible variable. The presented PE/atom histograms for Al spheres show that a known PE/atom threshold exists as a predictor of disordering like that observed in simulations of other materials deformed at high strain rates. The results presented in this study are relevant in considering both high velocity particle impact and indentation by small indenters at high strain rates.

CRediT authorship contribution statement

Tanish Kothapalle: Writing – review & editing, Writing – original draft, Visualization, Software, Methodology, Investigation, Formal analysis, Data curation. Aneesh V. Melachuri: Writing – review & editing, Writing – original draft, Visualization, Methodology, Investigation, Formal analysis, Data curation. James J. Rogers: Writing – review & editing, Writing – original draft, Visualization, Software, Methodology, Investigation, Data curation. Kien Bach Tran: Writing – review & editing, Writing – original draft, Visualization, Software, Methodology, Investigation, Formal analysis, Data curation. Michael F. Becker: Writing – review & editing, Writing – original draft, Supervision, Software, Resources, Methodology, Investigation, Funding acquisition, Data curation, Conceptualization. Desiderio Kovar: Writing – review & editing, Writing – original draft, Validation, Supervision, Resources, Project administration, Methodology, Investigation, Funding acquisition, Formal analysis, Conceptualization.

Declaration of competing interest

The authors declare that they have no known competing financial interests or personal relationships that could have appeared to influence the work reported in this paper.

Data availability

Data will be made available on request.

Acknowledgments

This work was supported by the National Science Foundation under Grant No. CMMI 2102818. Kothapalle, Melachuri, Rogers, and Tran acknowledge support and participation in the freshman introduction to research in engineering (FIRE) course provided by the Walker Department of Mechanical Engineering. The authors acknowledge the Texas Advanced Computing Center (TACC) at The University of Texas at

Austin for providing high-performance computing resources that have contributed to the research results reported within this paper. URL: http://tacc.utexas.edu.

References

- J.T.M. De Hosson, W.A. Soer, A.M. Minor, Z. Shan, E.A. Stach, S.A. Syed Asif, O. L. Warren, In situ TEM nanoindentation and dislocation-grain boundary interactions: a tribute to David Brandon, J. Mater. Sci. 41 (2006) 7704–7719.
- [2] K.A. Rzepiejewska-Malyska, G. Buerki, J. Michler, R.C. Major, E. Cyrankowski, S.A. S. Asif, O.L. Warren, In situ mechanical observations during nanoindentation inside a high-resolution scanning electron microscope, J. Mater. Res. 23 (2008) 1973–1979
- [3] J. Lu, S. Suresh, G. Ravichandran, Dynamic indentation for determining the strain rate sensitivity of metals, J. Mech. Phys. Solids 51 (2003) 1923–1938.
- [4] Y. Gao, C.J. Ruestes, H.M. Urbassek, Nanoindentation and nanoscratching of iron: atomistic simulation of dislocation generation and reactions, Comput. Mater. Sci 90 (2014) 232–240.
- [5] D. Mordehai, M. Kazakevich, D.J. Srolovitz, E. Rabkin, Nanoindentation size effect in single-crystal nanoparticles and thin films: a comparative experimental and simulation study, Acta Mater. 59 (2011) 2309–2321.
- [6] M. Hassani, D. Veysset, K. Nelson, C. Schuh, In-situ observations of single microparticle impact bonding, Scr. Mater. 145 (2017) 9–13.
- [7] W. Xie, A. Alizadeh-Dehkharghani, Q. Chen, V.K. Champagne, X. Wang, A.T. Nardi, S. Kooi, S. Müftü, J.-H. Lee, Dynamics and extreme plasticity of metallic microparticles in supersonic collisions, Sci. Rep. 7 (2017) 5073.
- [8] H. Haberland, Z. Insepov, M. Karrais, M. Mall, M. Moseler, Y. Thurner, Thin film growth by energetic cluster impact (ECI): comparison between experiment and molecular dynamics simulations, Mat. Sci. Eng. B 19 (1993) 31–36.
- [9] H. Hsieh, R.S. Averback, H. Sellers, C.P. Flynn, Molecular-dynamics simulations of collisions between energetic clusters of atoms and metal substrates, Phys. Rev. B 45 (1992) 4417–4430.
- [10] A. Tolvanen, K. Albe, Plasticity of Cu nanoparticles: dislocation-dendrite-induced strain hardening and a limit for displacive plasticity, Beilstein J. Nanotechnol. 4 (2013) 173–179.
- [11] T.V. Chitrakar, J.W. Keto, M.F. Becker, D. Kovar, Particle deposition and deformation from high speed impaction of Ag nanoparticles, Acta Mater. 135 (2017) 252–262.
- [12] T.V. Chitrakar, M.F. Becker, D. Kovar, A quantitative criterion to predict atomic disordering during high velocity nanoparticle impact, J. Aero. Sci. 165 (2022) 106042.
- [13] T.V. Chitrakar, M.F. Becker, D. Kovar, Influence of crystallographic orientation on the deformation of Ag nanoparticles during high-speed impact, J. Therm. Spray. 32 (2023) 2683–2700.
- [14] P.S. Branício, J.-P. Rino, Large deformation and amorphization of Ni nanowires under uniaxial strain: a molecular dynamics study, Phys. Rev. B 62 (2000) 16950–16955.
- [15] H. Tsuzuki, J.P. Rino, P.S. Branicio, Dynamic behaviour of silicon carbide nanowires under high and extreme strain rates: a molecular dynamics study, J. Phys. D: Appl. Phys. 44 (2011) 055405.
- [16] M.F. Becker, D. Kovar, A quantitative criterion for predicting solid-state disordering during high strain rate deformation, J. Phys. Condens. Matter 33 (2020) 065405.
- [17] M.F. Becker, D. Kovar, A quantitative criterion for predicting solid-state disordering during biaxial, high strain rate deformation, Modelling Simul. Mater. Sci. 30 (2021) 015006.
- [18] S. Plimpton, Fast parallel algorithms for short-range molecular dynamics, J. Comp. Phys. 117 (1995) 1–19.
- [19] P.L. Williams, Y. Mishin, J.C. Hamilton, An embedded-atom potential for the Cu–Ag system, Model. Simul. Mater. Sci. Eng. 14 (2006) 817–833.
- [20] V.V. Zhakhovskii, N.A. Inogamov, Y.V. Petrov, S.I. Ashitkov, K. Nishihara, Molecular dynamics simulation of femtosecond ablation and spallation with different interatomic potentials, Appl. Surf. Sci. 255 (2009) 9592–9596.
- [21] W. Shinoda, M. Shiga, M. Mikami, Rapid estimation of elastic constants by molecular dynamics simulation under constant stress, Phys. Rev. B 69 (2004) 134103.
- [22] A. Stukowski, Visualization and analysis of atomistic simulation data with OVITO the open visualization tool, Modelling Simul. Mater. Sci. Eng. 18 (2010) 015012.
- [23] C.M. Larson, J.J. Choi, P.A. Gallardo, S.W. Henderson, M.D. Niemack, G. Rajagopalan, R.F. Shepherd, Direct ink writing of silicon carbide for microwave optics, Adv. Eng. Mater. 18 (2016) 39–45.
- [24] A. Stukowski, V.V. Bulatov, A. Arsenlis, Automated identification and indexing of dislocations in crystal interfaces, Modelling Simul. Mater. Sci. 20 (2012) 085007.
- [25] T.C. Germann, B.L. Holian, P.S. Lomdahl, D. Tanguy, M. Mareschal, R. Ravelo, Dislocation structure behind a shock front in fcc perfect crystals: atomistic simulation results, Metall. Mater. Trans. A 35 (2004) 2609–2615.
- [26] W.-W. Pang, P. Zhang, G.-C. Zhang, A.-G. Xu, X.-G. Zhao, Dislocation creation and void nucleation in FCC ductile metals under tensile loading: a general microscopic picture, Sci. Rep. 4 (2014) 6981.
- [27] C.E. Carlton, P.J. Ferreira, In situ TEM nanoindentation of nanoparticles, Micron 43 (2012) 1134–1139.